Journal of Materials Chemistry C

ROYAL SOCIETY OF CHEMISTRY

PAPER

View Article Online
View Journal | View Issue

Cite this: J. Mater. Chem. C, 2021, 9, 10414

Greatly enhanced dielectric charge storage capabilities of layered polymer composites incorporated with low loading fractions of ultrathin amorphous iron phosphate nanosheets†

Meiyu Zhang,[a] Zhicheng Shi,[a]* Jifu Zhang,[a] Kun Zhang,[b] Li Lei,[a] Davoud Dastan[c] and Bohua Dong[a]*

Received 29th April 2021,
Accepted 5th July 2021

DOI: 10.1039/d1tc01974k

rsc.li/materials-c

Two-dimensional nanomaterials are promising fillers for dielectric nanocomposites because of their high specific surface areas which can induce strong interfacial polarization and result in improved dielectric permittivity. In this work, ultrathin amorphous $FePO_4$ nanosheets with a thickness of about 3.7 nm are successfully obtained using a one-step solvothermal method and are further dispersed into a P(VDF–HFP) matrix, forming $FePO_4$/P(VDF–HFP) nanocomposites. Obviously enhanced dielectric permittivities are achieved owing to the strong interfacial polarization at the huge interfaces between the $FePO_4$ nanosheets and the P(VDF–HFP) matrix. A greatly enhanced dielectric permittivity of 18.5@10 kHz, which is about 240% that of the P(VDF–HFP) matrix, is obtained in the composite with merely 2 wt% $FePO_4$ nanosheets. Furthermore, bilayer paraelectric/ferroelectric composites, in which pure polyetherimide acts as the paraelectric layer and the $FePO_4$/P(VDF–HFP) composite as the ferroelectric layer, are fabricated. It is found that, the synergistic effect between the two layers results in a substantially suppressed loss and elevated breakdown strengths, as well as obviously improved energy density and discharge efficiency in comparison with the single layer $FePO_4$/P(VDF–HFP) composites. Consequently, a high energy density of 7.58 J cm^{-3} and a high discharge efficiency of 81.6% are concurrently achieved in the bilayer composite with merely 0.5 wt% $FePO_4$ nanosheets. The excellent dielectric energy storage performances make these composites promising candidates for advanced electrostatic capacitors.

1. Introduction

Electrostatic capacitors, which have ultrahigh power density,[1] excellent self-healing capability,[2] fast charge–discharge rate[3,4] and long cycle lifetime,[5] are widely employed in various pulsed power systems, including electric transport systems, high-power weapons, medical equipment,[6,7] *etc.* However, the application of capacitors is greatly limited by their low energy storage densities. Energy density is an important parameter that reflects the energy storage capacity of a dielectric material and is generally expressed as $U = \int E\mathrm{d}D$, where U is the energy density, E is the applied electric field, and D is the electric displacement. Particularly, the energy density of a linear material can be simplified as $U = 1/2\varepsilon_0\varepsilon_r E^2$, where ε_0 is the vacuum dielectric permittivity (8.85×10^{-12} F m^{-1}) and ε_r is the relative dielectric permittivity of the material.[8] Accordingly, in order to obtain a higher energy density, materials with high dielectric permittivity and high breakdown strength are desired.

To achieve high ε_r, various strategies have been proposed, among which constructing polymer nanocomposites composed of inorganic nanofillers dispersed in the polymer matrix is the most widely adopted one. The dielectric performance of the polymer nanocomposite is greatly determined by the type of nanofiller. Taking the two most widely used fillers (*i.e.*, conductive fillers and ferroelectric ceramic fillers) for example, the addition of conductive fillers (*e.g.*, metal, carbon, conductive ceramic, *etc.*) can result in a sharply elevated ε_r near the percolation threshold, while only limited dielectric enhancement can be achieved when ferroelectric ceramics are adopted as the fillers.[9,10] In addition, the morphology of fillers also plays crucial roles in determining the dielectric performances of the composites. Generally, nanofillers can be classified into three types according to their morphologies: zero-dimensional (0D)

[a] School of Materials Science and Engineering, Ocean University of China, Qingdao 266100, P. R. China. E-mail: zcshi@ouc.edu.cn, dongbohua@ouc.edu.cn
[b] Key Laboratory of Microgravity (National Microgravity Laboratory), Institute of Mechanics, Chinese Academy of Sciences, Beijing 100190, China
[c] Department of Materials Science and Engineering, Georgia Institute of Technology, Atlanta, Georgia, 30332, USA

† Electronic supplementary information (ESI) available. See DOI: 10.1039/d1tc01974k

nanofillers (*e.g.*, nanospheres and nanodots),[11–14] one-dimensional (1D) nanofillers (*e.g.*, nanotubes and nanofibers)[15–17] and two-dimensional (2D) nanofillers (nanosheets).[18,19] Among them, 2D nanofillers are believed to be the most promising candidates for dielectric energy storage composites. In the composites filled with 2D nanofillers, numerous micro-lamellar structures will be formed. When the 2D nanofillers are electrically insulating, the micro-lamellar structure can effectively block the development of the leakage conductive paths, thereby increasing the breakdown strength and energy storage density.[20–22] When the 2D nanofillers are electrically conductive or semi-conductive, the micro-lamellar structure can form numerous equivalent microcapacitors under external electric fields, yielding enhanced dielectric permittivity and energy density.[19,23,24] Chen[25] and coworkers fabricated a series of poly(vinylidene fluoride) (PVDF) based composites containing 2D boron nitride nanosheets (BNNS) with excellent electric insulating properties. An obviously enhanced breakdown strength of 334 MV mm^{-1}, which is about 160% that of a pure PVDF matrix, is achieved in the composite with merely 3 vol% BNNS. As a result, a high energy density of 9.9 J cm^{-3} and a satisfactory efficiency of 68.3% are realized. Ji[26] and coworkers prepared three types of $Ni(OH)_2$ nanoparticles with different morphologies, including 0D nanospheres, 2D nanoplatelets, and 3D nanoflowers. Then the dielectric properties of PVDF based composites incorporated with these nanofillers were compared. It is demonstrated that, to achieve comparable dielectric performance, the required loading fraction of 2D nanoplatelets is much lower than that of 0D nanospheres and 3D nanoflowers. Consequently, a high dielectric permittivity of 16.3 and a high energy density of 17.3 J m^{-3} are achieved in the composite with merely 3.02 vol% 2D $Ni(OH)_2$ nanoplatelets.

In this work, ultrathin ($\sim$3.7 nm) amorphous iron phosphate nanosheets ($FePO_4$) are synthesized by a facile one-step solvothermal method, and are incorporated as fillers into a poly(vinylideneuoride–hexa-uoropropylene) (P(VDF–HFP)) matrix, forming $FePO_4$/P(VDF–HFP) nanocomposites. The ultrathin $FePO_4$ nanosheets possess high specific surface area, which offers abundant sites for charge storage under external electric fields. In addition, there exist a huge amount of coordination defects in the amorphous $FePO_4$ nanosheets because of their disordered microstructure. And the defects will result in the asymmetric distribution of electrons around them, forming equivalent dipoles which will strengthen the dipolar polarization and enhance the dielectric permittivity. Besides, the radial conductivity of the amorphous nanosheets is usually very low, which is beneficial for depressing the leakage conduction loss. As a result, the introduction of $FePO_4$ nanosheets results in obviously enhanced dielectric permittivities and energy densities in comparison with those of the pure P(VDF–HFP) matrix. Furthermore, to suppress the loss and achieve a higher discharge efficiency, ferroelectric $FePO_4$/P(VDF–HFP) nanocomposites are hot pressed with paraelectric polyetherimide (PEI), forming bilayer $FePO_4$/P(VDF–HFP)–PEI nanocomposites. As a result, in comparison with single layer $FePO_4$/P(VDF–HFP) nanocomposites, bilayer composites exhibit greatly suppressed loss and improved breakdown strengths, as well as simultaneously enhanced energy densities and discharge efficiencies. A high breakdown strength of 472.24 kV mm^{-1}, a high energy density of 7.58 J cm^{-3} and a high discharge efficiency of 81.6% are concurrently obtained in the bilayer composite with merely 0.5 wt% $FePO_4$ nanosheets. To the best of our knowledge, this is the first report of the application of $FePO_4$ nanosheets in dielectric nanocomposites. The outstanding comprehensive energy storage performances make these nanocomposites promising candidates for advanced electrostatic capacitors.

2. Experimental

2.1. Materials

Poly(vinylidene fluoride–hexafluoropropylene) (P(VDF–HFP), 15% HFP, PolyK Technologies, USA), poly-etherimide (PEI, PolyK Technologies, USA), 1-methyl-2-pyrrolidone (C_5H_9NO, 99.0% Sinopharm Chemical Reagent Co., Ltd), sodium dodecylbenzenesulfonate ($C_{18}H_{29}NaO_3$, 88.0%, Sinopharm Chemical Reagent Co., Ltd) and ethanol (99.7%, Sinopharm Chemical Reagent Co., Ltd), iron nitrate nonahydrate ($Fe(NO_3)_3{\cdot}9H_2O$), oleylamine (OAm, C18: 80–90%) and 1-octadecene (ODE, >90.0%) were purchased from the Aladdin Reagent Co. Ltd. Sodium phosphate monobasic dehydrate ($NaH_2PO_4{\cdot}2H_2O$) was purchased from the Sinopharm Chemical Reagent Co. Ltd. All chemicals were used as received without further purification. All aqueous solutions were prepared using deionized water with a resistivity of 18.2 MΩ cm^{-1}.

2.2. Synthesis of amorphous $FePO_4$ nanosheets

Amorphous $FePO_4$ nanosheets were synthesized through a one-step solvothermal process. In detail, 1 mmol Fe $(NO_3)_3{\cdot}9H_2O$ was dissolved in a mixture of oleylamine (3 mL) and 1-octadecene (10 mL) under constant stirring for 30 min. Then 0.2 M aqueous $NaH_2PO_4{\cdot}2H_2O$ solution (10 mL) was added into the above mixture. Subsequently, the mixed solution was transferred into a Teflon-lined autoclave and heated at 180 °C for 24 h in an electric oven. After cooling to room temperature, the as-obtained products were washed with cyclohexane and ethanol several times using centrifugation followed by a drying treatment at 60 °C for 12 h (Fig. 1).

2.3. Preparation of bilayer composites

First, the $FePO_4$/P(VDF–HFP) suspension and PEI solution were prepared. For the preparation of $FePO_4$/P(VDF–HFP) suspension, $FePO_4$ particles and sodium dodecylbenzene sulfonate (SDBS) were ultrasonically dispersed in 5 mL of 1 methyl-2-pyrrolidone (NMP) for 1.5 h at room temperature. Then the P(VDF–HFP) particles are added to the suspension under magnetic stirring at 75 °C until the P(VDF–HFP) particles are completely dissolved, yielding the $FePO_4$/P(VDF–HFP) suspension. Similarly, to prepare the PEI solution, PEI particles were directly dissolved in 1-methyl-2-pyrrolidone (NMP) followed by stirring rapidly at 75 °C for 5 h and gently overnight at room temperature. Subsequently, the $FePO_4$/P(VDF–HFP) suspension and PEI solution were casted on glass plates followed by drying at 100 °C for 4 h and 200 °C for 5 min. After that, the films were peeled off by quenching in ice water and dried in an oven at

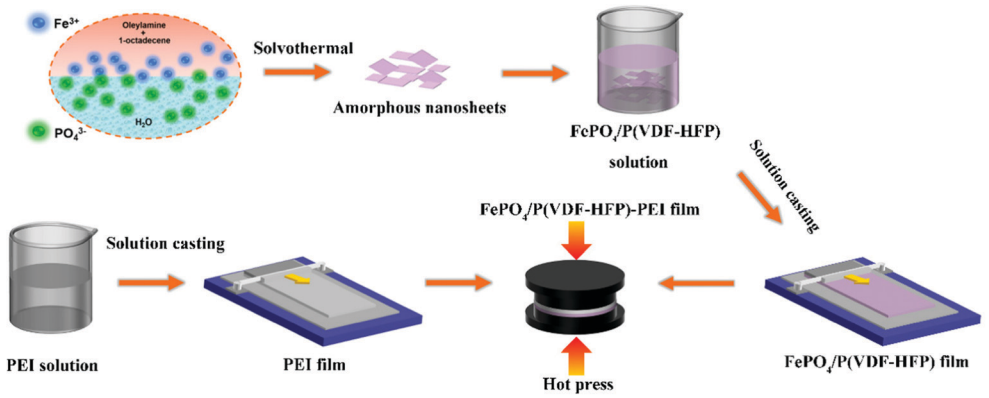

Fig. 1 Schematic fabrication process of the bilayer $FePO_4$/P(VDF–HFP)–PEI nanocomposites.

70 °C for 6 h to obtain single layer (1L) $FePO_4$/P(VDF–HFP) composite films and PEI films. The thickness of the films is controlled to be approximately 15 μm by adjusting the height of the blades. Finally, $FePO_4$/P(VDF–HFP)–PEI bilayer (2L) films were fabricated by hot pressing the stacked $FePO_4$/P(VDF–HFP) and PEI films at 170 °C under a pressure of 10 MPa.

2.4. Characterization and measurements

The microstructure and morphology of the $FePO_4$ samples were characterized with a transmission electron microscope (TEM, JEOL, JEM 1200) and a high-resolution TEM (HRTEM, FEI Tecnai G2 F20). A Bruker Dimension Icon atomic force microscope (AFM) was used to determine the thickness of the nanosheets. X-Ray diffraction (XRD) patterns were obtained using a Bruker D8 Advance X-ray diffractometer equipped with a Cu Kα source. X-Ray photoelectron spectroscopy (XPS) spectra were recorded on a Thermo ESCALAB 250Xi photoelectron spectrometer. The morphologies and elemental distributions of the bilayer films were observed by scanning electron microscopy (SEM, Gemini300, ZEISS, Ltd) combined with EDX (INCA, Oxford, Ltd). Fourier-transform infrared (FTIR) spectra were obtained using a Nicolet iS5 FTIR instrument from 3900 cm^{-1} to 400 cm^{-1}. Circular gold electrodes with a diameter of 2.98 mm were sputtered on the two sides of the samples before dielectric measurements. The dielectric properties were analyzed with an Agilent E4980A Precision LCR analyzer in the frequency range from 100 Hz to 1 MHz. Open and short compensations were performed before testing. The permittivity was calculated using $\varepsilon_r = TC_m/A\varepsilon_0$, where T is the thickness of the sample, f is the electric field frequency, A is the area of the electrode, C_m is the parallel capacitance, and ε_0 is the absolute permittivity of free space (8.85×10^{-12} F m^{-1}). The variation of leakage current density with electric field (J–E loop) was measured using a source meter (2400, Keithley Instruments). The breakdown strengths were obtained using a setup equipped with a Trek 609A amplifier with a voltage ramping rate of 500 V s^{-1} at room temperature (PolyK Technologies, USA). The extended path of breakdown is observed using a metallurgical microscope (Lab.A1, ZEISS, Ltd). The energy storage performances (*e.g.*, discharge energy densities, discharge efficiencies, maximum and remnant polarization) were obtained using P–E hysteresis loops which were collected using a ferroelectric test system based on a modified Sawyer–Tower circuit (PolyK Technologies, USA). The fast charge/discharge tests were carried out through a PK-CPR1502 test system (Polyk Technologies) and a Trek Model 20/20C ±20 kV high voltage amplifier system with a load resistor (RL) of 10 kΩ.

3. Results and discussion

The transparent transmission electron microscopy (TEM) image (Fig. 2a) indicates that the $FePO_4$ nanosheets exhibit a 2D ellipse nanosheet morphology with a lateral size of ~800 nm (for more TEM observation of nanosheets, please find in Fig. S1a, ESI†). The high-resolution TEM (HRTEM) image reveals that the as-synthesized $FePO_4$ nanosheet is amorphous, evidenced by the absence of typical lattice fringes (Fig. 2b), in agreement with the selected-area electron diffraction image (inset of Fig. 2a) and the FFT pattern (inset of Fig. 2b). The wide-angle XRD pattern (Fig. S1b, ESI†) with no obvious diffraction peaks further confirms the amorphous feature of the $FePO_4$ ultrathin nanosheet. The specific thickness of the $FePO_4$ ultrathin nanosheets was determined to be 3.7 nm by atomic force microscopy (AFM) (Fig. 2c). The composition of the 2D $FePO_4$ nanosheets was determined using the X-ray photoelectron spectroscopy (XPS) survey spectra (Fig. S1c, ESI†). The cross-sectional SEM images of the 2 wt% $FePO_4$/P(VDF–HFP)–PEI bilayer composite and PEI film are shown in Fig. 2d and Fig. S1d (ESI†). We can see that the composite film is of high quality without any obvious holes or voids, and the distribution of F element clearly confirms the double-layer structure. Moreover, the specific EDX elemental content is given in Fig. S2 (ESI†), and no obvious Fe element signals are observed which should be attributed to the ultralow filling fractions of $FePO_4$ nanosheets.

The FTIR spectra of pure P(VDF–HFP), PEI and $FePO_4$/P(VDF–HFP) composite films with different $FePO_4$ contents are shown in Fig. 3. The typical characteristic absorption peaks of PEI can be clearly observed. The absorption peaks at wave numbers of 1777 cm^{-1} and 1712 cm^{-1} originate from the

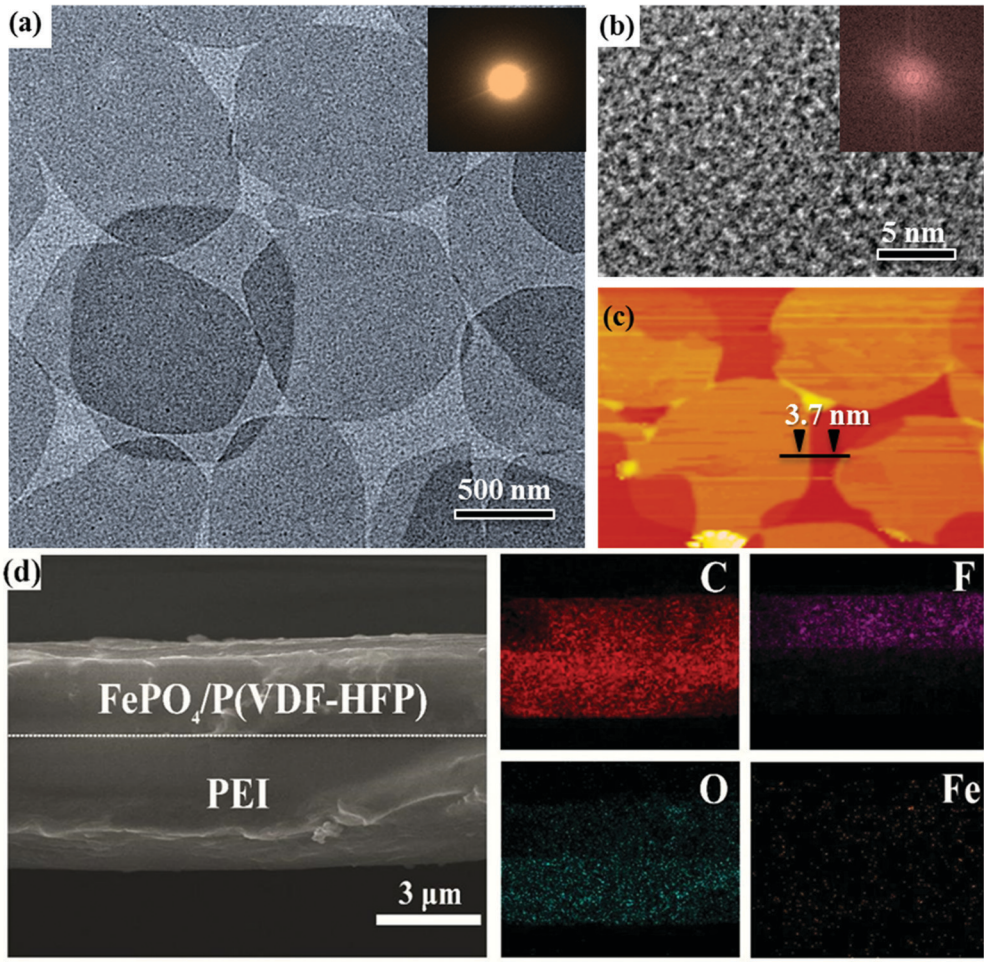

Fig. 2 (a) TEM image of $FePO_4$. (b) HRTEM image of representative $FePO_4$. The insets of (a) and (b) show the selected-electron diffraction and FFT patterns of amorphous $FePO_4$, respectively. (c) AFM image of $FePO_4$; the thickness is about 3.7 nm. (d) Cross-sectional SEM images and elemental mapping of the bilayer $FePO_4$/P(VDF–HFP)–PEI composites.

asymmetric stretching vibrations and symmetric stretching vibrations of the carbonyl group of the polyetherimide ring, respectively.[27,28] The absorption peak at 1370 cm^{-1} represents the carbon–nitrogen bond (C–N) in the polyetherimide ring, and the absorption peak at 725 cm^{-1} is the flexural vibration of the carbonyl group of the polyetherimide ring.[29] The α and β phases of PVDF also existed in the P(VDF–HFP) copolymer, and these phases were formed by the VDF segments in the copolymer.[30] The absorption peaks at wavenumbers of 488 cm^{-1}, 615 cm^{-1}, 762 cm^{-1} and 1383 cm^{-1} indicate the formation of the α phase in P(VDF–HFP), while the peak at 874 cm^{-1} demonstrates the formation of the β phase in P(VDF–HFP).[31] The peaks observed around 1060 cm^{-1} and 1178 cm^{-1} correspond to the symmetric stretching mode of CF_2.[31] The FTIR results demonstrate that the addition of $FePO_4$ does not obviously affect the structure of P(VDF–HFP).

The frequency dependences of dielectric permittivity and loss tangent for PEI, P(VDF–HFP), and single layer (1L) and bilayer (2L) composites are displayed in Fig. 4. As seen, the pure PEI film shows the lowest permittivity and is almost independent of frequency in the tested frequency range because of its intrinsic paraelectric characteristics. In contrast, the pure P(VDF–HFP) has a much higher permittivity than pure PEI

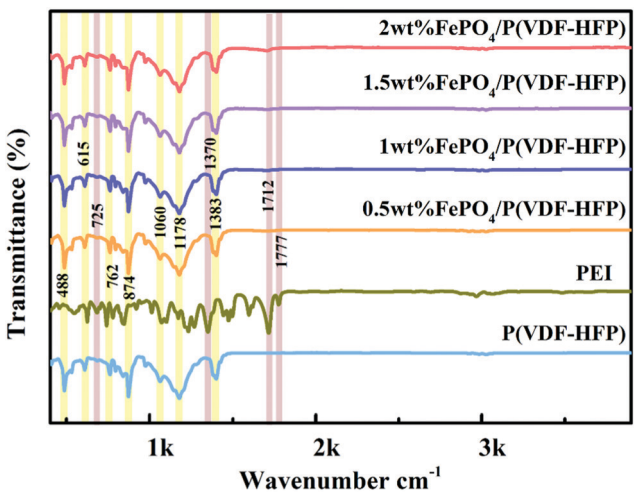

Fig. 3 FTIR spectra of pure P(VDF–HFP), pure PEI, and $FePO_4$/P(VDF–HFP) nanocomposites.

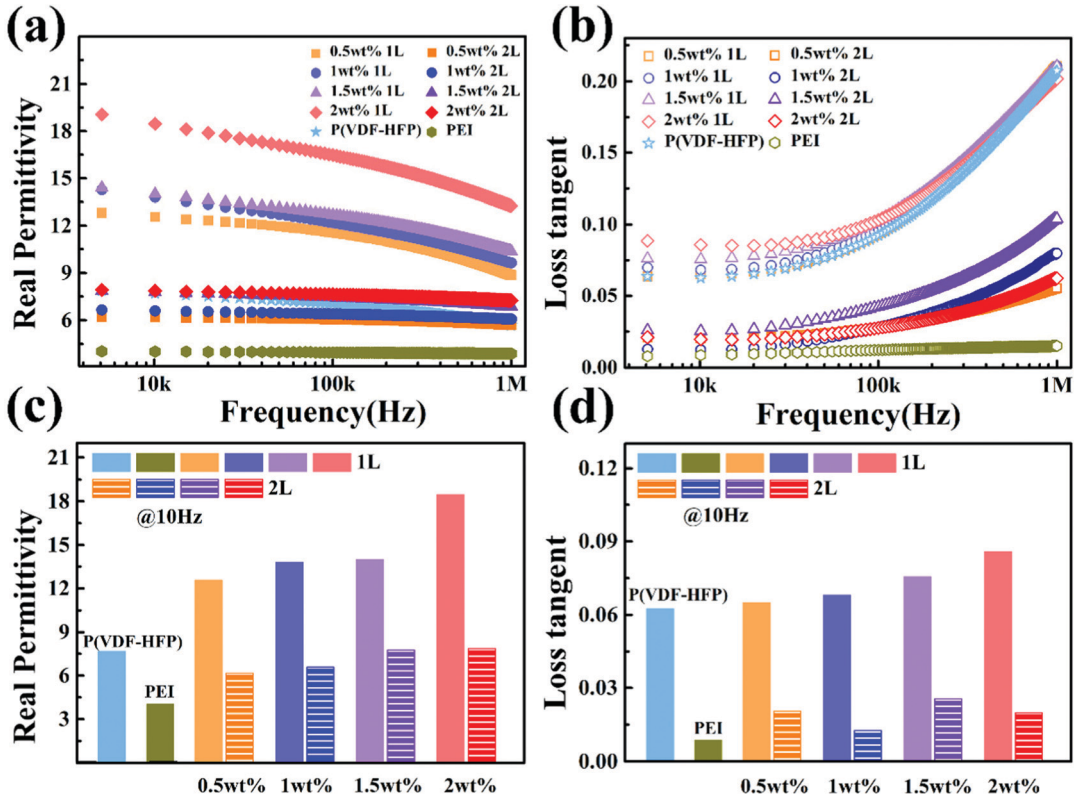

Fig. 4 The frequency dependence of dielectric permittivity (a) and loss tangent (b) of single layer and bilayer nanocomposites. The variation of dielectric permittivity (c) and loss tangent (d) with $FePO_4$ loading fractions for the single layer and bilayer nanocomposites.

and exhibits apparent frequency dispersion behavior owing to its intrinsic ferroelectric characteristic. It can also be found that the incorporation of $FePO_4$ nanosheets into the P(VDF–HFP) results in obviously enhanced dielectric permittivity and the dielectric permittivities increase with the increasing content of $FePO_4$. Specifically, the composite with merely 2 wt% $FePO_4$ nanosheets exhibits a high dielectric permittivity of 18.5@10 kHz, which is approximately 240% that of the pure P(VDF–HFP) (~7.7@10 kHz). The significantly enhanced dielectric permittivity is due to the strengthened Maxwell–Wagner–Sillars interfacial polarization at the ultra-large interfaces between $FePO_4$ nanosheets and the P(VDF–HFP) matrix. At the same time, the charge polarization of $FePO_4$ driven by an external electric field also contributes to the improved dielectric permittivity. The results demonstrate that $FePO_4$ nanosheets are excellent candidates for composites with high dielectric permittivity. Compared to the dielectric performances of the 1L and 2L composites, we can conclude that the 2L composites possess much lower dielectric permittivities and loss than the 1L composites. This phenomenon originates from the inherent low dielectric permittivity and low loss of the PEI layer. In practical applications, the low loss is beneficial to the long-term operation of the capacitor with low dissipation heat.

In addition to dielectric permittivity, the breakdown strength also plays crucial roles in determining the energy storage performances of a dielectric material. Therefore, the breakdown behaviors of the composites are further studied. The tested breakdown electric fields of the composites are analyzed using the two-parameter Weibull distribution formula, which can be described as:

$$P(E) = 1 - \exp(-(E/E_b)^{\beta}) \quad (1)$$

where $P(E)$ is the cumulative probability of failure, E represents the actual breakdown strength obtained from the experimental test, E_b represents the breakdown strength value of 63.2% cumulative failure probability, and β is the shape parameter which evaluates the dispersion of the data (*i.e.*, the larger the β value, the better the distribution of breakdown strengths). The Weibull distribution of the breakdown strengths of the nanocomposites with varied $FePO_4$ fractions is shown in Fig. 5a and Fig. S3 (ESI†). We can see that all of the composites show high β values (see Fig. S3, ESI†), indicating the high reliability of the tested results. As shown in Fig. 5(a and b), the pure PEI has the highest E_b of 562.53 kV mm^{-1} and pure P(VDF–HFP) also exhibits a high E_b of 463.89 kV mm^{-1}. Moreover, the 1L $FePO_4$/P(VDF–HFP) composites display suppressed E_b in comparison with pure P(VDF–HFP). The suppressed E_b should be attributed to two reasons: (1) the $FePO_4$ has higher conductivity than P(VDF–HFP), which could result in enhanced leakage conduction (see Fig. S4, ESI†); (2) there may exist structural defects (*e.g.*, voids and agglomeration of $FePO_4$ nanosheets) in the composites, and electrical tree branches will grow along the direction of the defect, which reduces the breakdown resistance of the composites. It is worth noting that the 2L composites

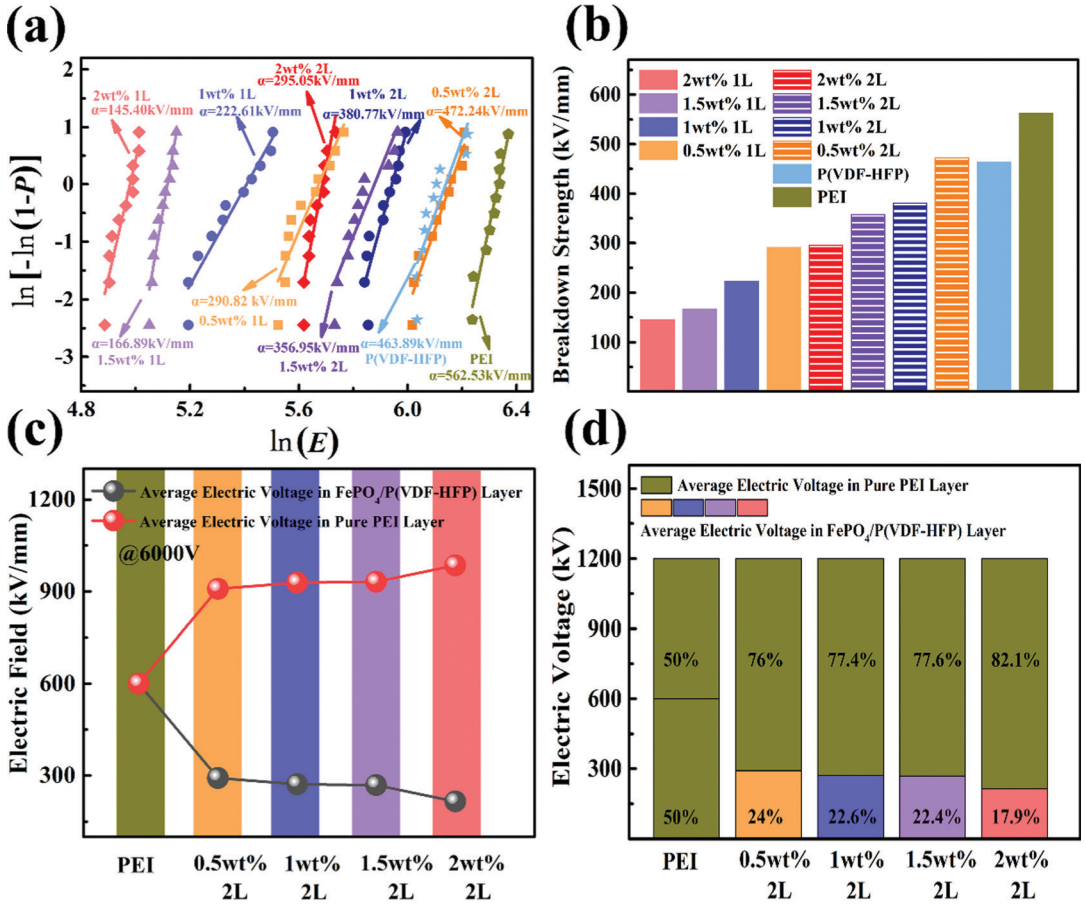

Fig. 5 Weibull distribution diagram (a) and characteristic breakdown strengths (b) of single layer and bilayer composites with different $FePO_4$ loading fractions. (c) The average electric field of different layers of the bilayer $FePO_4$/P(VDF–HFP)–PEI nanocomposite at 6000 V calculated by using the series capacitor model. (d) The percentage of the average electric voltages in different layers of the bilayer $FePO_4$/P(VDF–HFP)–PEI nanocomposite.

show remarkably improved E_b compared with their 1L counterparts. Specifically, the E_b values of the 2L composites with 0.5 wt%, 1 wt%, 1.5 wt%, and 2 wt% $FePO_4$ are 162%, 171%, 214% and 203% those of their 1L counterparts. Particularly, the bilayer composite with 0.5 wt% $FePO_4$ exhibits an outstanding E_b of 472.2 kV mm^{-1}, which is even higher than that of pure P(VDF–HFP). It is believed that due to the contrast between the dielectric permittivities in the different layers, more applied voltage will be concentrated on the lower dielectric permittivity layer, thereby protecting the high dielectric permittivity layer from damage. To verify this hypothesis, we managed to establish a simple series capacitor model, which is composed of two series capacitors representing the $FePO_4$/P(VDF–HFP) layer and PEI layer, respectively. And the applied voltages on the two layers are calculated by the following formula:

$$E_s = V \Big/ \left(d_s + d_h\left(\frac{\varepsilon_s}{\varepsilon_h}\right)\right); \quad E_h = V \Big/ \left(d_h + d_s\left(\frac{\varepsilon_h}{\varepsilon_s}\right)\right) \quad (2)$$

where V is the applied voltage on the entire nanocomposite, E_s is the applied electric field on the PEI layer, E_h is the applied electric field on the $FePO_4$/P(VDF–HFP) layer, d_s is the thickness of the PEI layer, d_h is the thickness of the $FePO_4$/P(VDF–HFP) layer, and ε is the dielectric permittivity. As shown in Fig. 5(c and d), the ratios of the electric field in different layers are calculated under an applied voltage of 6000 V (the total electric field is 400 kV mm^{-1}). In the 2L composite, although the $FePO_4$/P(VDF–HFP) layer is easily broken down, most of the applied voltage will be concentrated on the PEI layer with high E_b, thereby reducing the electric field in the $FePO_4$/P(VDF–HFP) layer. In addition, the electrical tree branches on the surface of the sample after breakdown are shown in Fig. S5 (ESI†). During the formation of electrical trees, the greater the bombardment energy of electrons, the easier it is to form electrical trees. As the voltage increases, the morphology of the electrical tree branches changes from sparse dendrites to dense dendrites, and finally to a jungle. Moreover, the huge electric field gap between the two layers can effectively prevent the development of the electrical tree, thereby preventing the electrical tree from penetrating the entire composite. And the electrical tree can develop along the interface between the adjacent layers, thereby increasing the length of the electrical tree development path and improving the breakdown strength.[32–34]

The energy storage capacities of nanocomposites are calculated based on the unipolar polarization–electric field (P–E) hysteresis loop. The typical unipolar loops of 1L and 2L composites with varying $FePO_4$ loading fractions are shown in

Fig. S6 and S7 (ESI†). We can see that the electric displacement increases as the electric field increases. The slim (or narrow) loop indicates that the deviation from the linear dielectric characteristics is small and corresponds to a low energy loss. As shown in Fig. 6a, the *P*–*E* loop of pure P(VDF–HFP) is much wider than that of pure PEI, indicating that the energy loss of P(VDF–HFP) is much higher than that of PEI during the charge/discharge process. Moreover, the 1L composites also show wide loops which are similar to those of pure P(VDF–HFP), indicating the high loss. It should be noted that, the 2L composites possess slim loops which are much narrower than their 1L counterparts and no serious broadening phenomenon is observed in the loops under elevated electric fields, indicating the low loss. Fig. 6b depicts the displacement of pure PEI, 1L and 2L composites with varying $FePO_4$ loading fractions at 180 kV mm^{-1}. The P_{max} value of $FePO_4$/P(VDF–HFP) composites increases with the increase of $FePO_4$ loading fraction. The P_{max} of $FePO_4$/P(VDF–HFP) composites with varied $FePO_4$ contents is much higher than that of P(VDF–HFP), while the P_r of $FePO_4$/P(VDF–HFP) composites is comparable to that of P(VDF–HFP). Consequently, the $FePO_4$/P(VDF–HFP) composites exhibit obviously elevated (P_{max}–P_r) compared with pure P(VDF–HFP), and this phenomenon should be attributed to the enhanced Maxwell–Wagner–Sillars interfacial polarization at the interfaces between $FePO_4$ and P(VDF–HFP). As for the 2L composites, under the same electric field, the addition of PEI reduces both the P_{max} and the P_r. Nevertheless, compared with pure PEI (0.6 μC cm^{-2}), the P_{max} of the bilayer composites has been

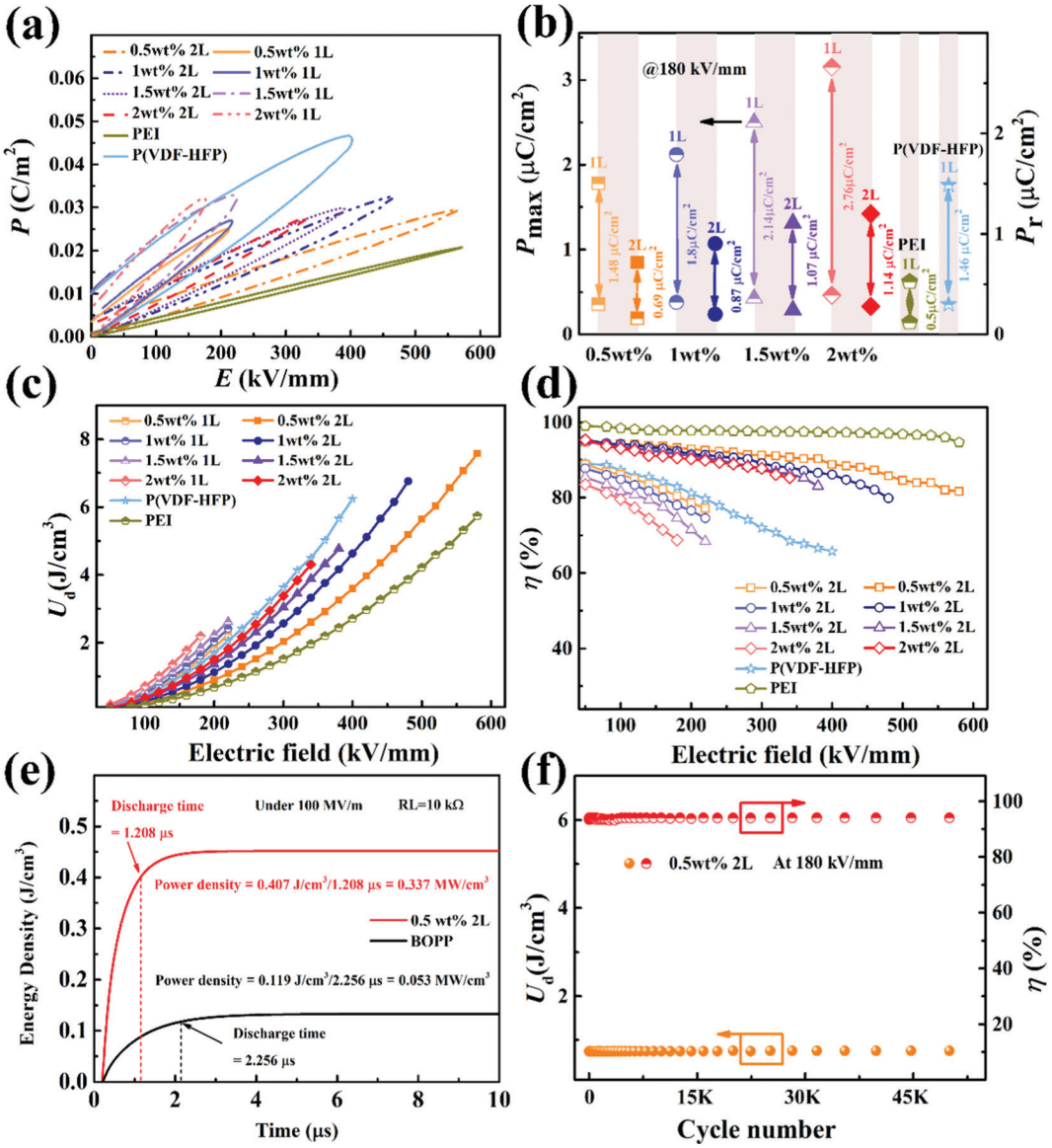

Fig. 6 *P*–*E* loops of (a) single layer and bilayer composites with different $FePO_4$ loadings. (b) The maximum displacement P_{max} and remnant displacement P_r of the pure PEI, single layer and bilayer composites at 180 kV mm^{-1}. (c) Discharged energy densities and (d) discharge efficiencies of the single layer and bilayer composites under varied external electric fields. (e) Fast charge/discharge performances of commercial BOPP and the 0.5 wt% 2L film. (f) The cycling stability of the energy density and efficiency of 0.5 wt% $FePO_4$/P(VDF–HFP)–PEI composites.

significantly improved, while the increase in P_r is quite slight, which results in an increase in the value of (P_{max}–P_r). The dielectric energy storage performances of the nanocomposites are further evaluated. The stored energy density (U_s) of the composites is obtained from the *P*–*E* loops by the area integral between the charge curve and the ordinate, while the discharged energy density (U_d) is obtained by integrating the area between the discharge curve and the ordinate, and the discharge efficiency η is calculated using the equation $\eta = U_d/U_s$. As shown in Fig. 6c and Fig. S8 (ESI†), under the same charge/discharge electric field, the PEI shows the lowest energy density, while the 1L composites exhibit the highest energy densities and the energy densities increase with an increasing $FePO_4$ content. That is to say, the $FePO_4$ nanosheets effectively improved the energy densities of the $FePO_4$/P(VDF–HFP) nanocomposites. For instance, the 1L composite with 2 wt% $FePO_4$ achieves a U_d of 2.2 J cm^{-3} at a charging electric field of 180 kV mm^{-1}, which is about 158% that of the pure P(VDF–HFP) matrix. These 1L composites can be promising candidates for low-voltage energy storage capacitors, but considering their low breakdown strengths, they cannot be used as high-voltage capacitors. In addition, their discharge efficiencies are low (<75% at 200 kV mm^{-1}, Fig. 6d), which will generate a large amount of loss and influence the performance stability. In contrast, although the 2L composites do not possess energy densities as high as their 1L counterparts under low electric fields, they can be charged to high voltages because of their high breakdown strengths which also endows the 2L composites with high energy densities. Meanwhile, the paraelectric characteristics and excellent insulating properties (Fig. S9, ESI†) of the PEI layer greatly suppress the loss during the charge/discharge process, which ensures high discharge efficiencies (>80% at 400 kV mm^{-1}, Fig. 6d). Particularly, the 2L composite with 0.5 wt% $FePO_4$ achieves a high U_d of 7.58 J cm^{-3} along with a high η of 81.6% at 580 kV mm^{-1}. Furthermore, the discharge behavior of the 2L composite with 0.5 wt% $FePO_4$ is evaluated. Specifically, the sample is charged at 100 MV m^{-1} and then discharged through a load resistance of 10 kΩ. The discharge time is described as the time for the U_d in a load resistor achieving 95% of the final value, and the power density is the ratio of U_d to discharge time. As displayed in Fig. 6e, biaxially oriented polypropylene (BOPP) has a U_d of 0.119 J cm^{-3} in 2.256 μs, while the 0.5 wt% 2L film releases 0.407 J cm^{-3} in 1.208 μs, which is 342% that of BOPP. The released energy density of the 0.5 wt% 2L film is consistent with the result of the *P*–*E* loops. Importantly, the 0.5 wt% 2L film shows an excellent released power density of 0.337 MW cm^{-3}, which is more than six times higher than that of the commercial BOPP film at 100 MV m^{-1} (0.053 MW cm^{-3}), indicating that the bilayer composite has great potential for applications in pulsed power systems.

The excellent comprehensive energy storage performances make the 2L composites good candidates for high-voltage capacitors. In practical applications, the cycling stability is also an important factor to be concerned. The charge and discharge energy densities as well as discharge efficiencies of the 2L composite with 0.5 wt% $FePO_4$ under continuous charge–discharge cycling processes are presented in Fig. 6f. It can be clearly seen that the composite shows no signs of degradation during the continuous 50 000 charge–discharge cycles, revealing the excellent cycling stability. As discussed above, the 2L composites possess superior η over the 1L composites and this difference should be mainly originated from the different loss behaviors. To elucidate the loss mechanism of the composites, the conduction loss is derived from the *P*–*E* loops with the assumption that the measured polarization at zero field ($P_{(E=0)}$) mainly comes from the leakage current, given that the ferroelectric films in this investigation contain insignificant contents of the polar phase.[35] The relationship between the effective conductivity σ_{eff} and $P_{(E=0)}$ can be derived as follows:

$$P_{(E=0)} = \sigma_{eff}/2E_{max}T \quad (3)$$

where σ_{eff} is the effective conductivity which represents the conduction loss, and T is the period of the applied field. After σ_{eff} is determined, the conduction loss can be subtracted from the total dielectric loss to obtain the ferroelectric loss. It is

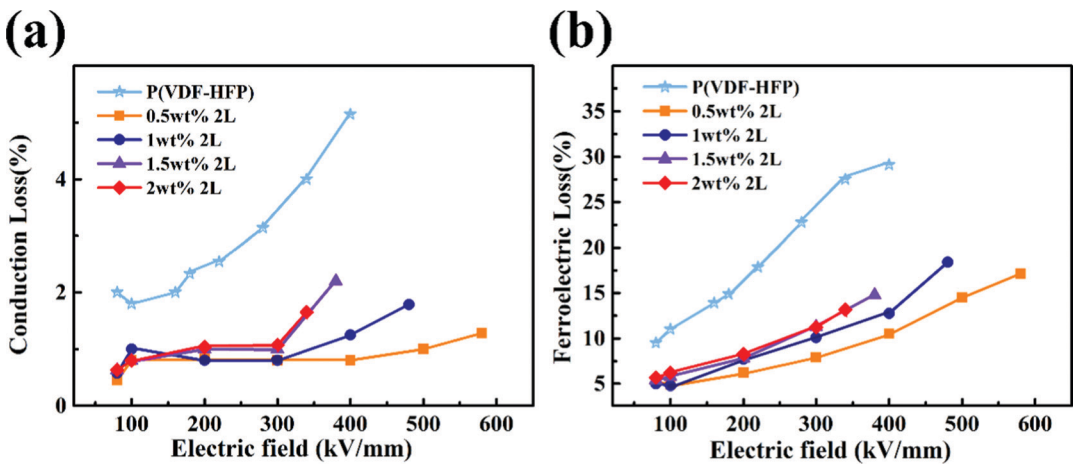

Fig. 7 Ferroelectric loss (a) and leakage conduction loss (b) of bilayer composite films under different electric fields.

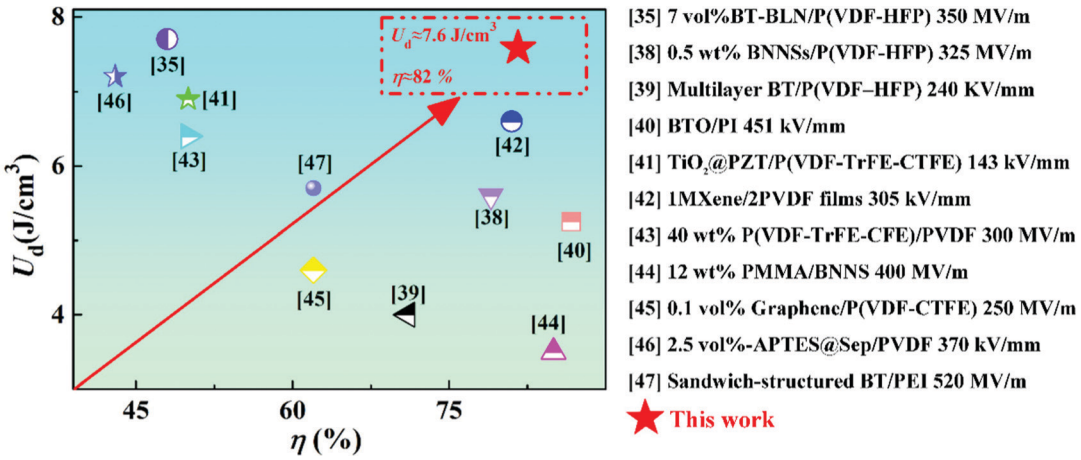

Fig. 8 Comparison of energy density and discharge efficiency of representative polymer-based nanocomposite dielectrics in the previous literature with this work.

believed that an increase in the filler content will reduce the distance and increase the interaction between adjacent fillers, resulting in an increased conduction loss and decreased efficiency. As displayed in Fig. 7, both the ferroelectric and conduction loss of the pristine P(VDF–HFP) films increase sharply with the increase of electric field, and the loss is dominated by ferroelectric loss. Similar variations of loss with the electric field are also observed in the 2L composites. In this work, there are no electric conductive fillers in the composite, so the proportion of conduction loss is very low. Moreover, as the electric field increases, the leakage conduction and the polarization strength increase, leading to the elevated conduction loss and ferroelectric loss. It is worth noting that the loss of the 2L films is much lower than that of pure P(VDF–HFP) under the same electric field. The suppressed conduction loss of the 2L composites should be ascribed to the excellent insulating properties of the PEI layer. Moreover, in the 2L composites, most of the electric voltage are applied on the paraelectric PEI layer, resulting in a lowered voltage on the ferroelectric P(VDF–HFP), hence the suppressed ferroelectric loss. In addition, the *J*–*E* data of 0.5 wt% 2L and PEI are fitted according to the hopping conduction model.[36,37] It can be seen from Fig. S9 (ESI†) that the *J*–*E* curve can basically be described by the hopping conduction equation. In other words, the main conduction mechanism of bilayer composites is hopping conduction. Moreover, the hopping distances are calculated from the fitted parameter *B* according to eqn (S2) (ESI†). The hopping distance increases from 0.46 nm of pure PEI to 0.53 nm of the 0.5 wt% 2L composite. Since the shorter hopping distance corresponds to a deeper trap depth,[36] the introduction of $FePO_4$ results in the reduced trap depth, hence the elevated leakage current loss.

Furthermore, the dielectric energy storage performances of the 2L composites are compared with those of other recently reported dielectric nanocomposites.[35,38–47] As illustrated in Fig. 8, it is difficult to achieve $U_d > 6$ J cm^{-3} and $\eta > 80\%$ simultaneously. Specifically, a high U_d is usually obtained in composites consisting of ferroelectric fillers hosted in a ferroelectric matrix,[35,41,43,46] while a high η is always realized in composites based on a paraelectric matrix.[40,44] In this work, $FePO_4$/P(VDF–HFP) composites that have high U_d are combined with PEI that has high η, yielding high U_d (7.58 J cm^{-3}) and η (81.6%) concurrently. The excellent comprehensive energy storage performances make these 2L composites promising candidates for advanced dielectric energy storage capacitors.

4. Conclusion

In summary, ultrathin amorphous $FePO_4$ nanosheets with a thickness of about 3.7 nm are synthesized by a one-step solvothermal method. Then the nanosheets are incorporated into the P(VDF–HFP) matrix, forming $FePO_4$/P(VDF–HFP) nanocomposites. It is found that the introduction of $FePO_4$ nanosheets results in obviously enhanced dielectric permittivity and energy density, which originate from the strong interfacial polarization that occurs at the huge interfaces between $FePO_4$ nanosheets and the P(VDF–HFP) matrix. Furthermore, to suppress the loss and achieve a higher discharge efficiency, the ferroelectric $FePO_4$/P(VDF–HFP) nanocomposites are hot pressed with paraelectric PEI, forming bilayer $FePO_4$/P(VDF–HFP)–PEI nanocomposites. As a result, in comparison with the single layer $FePO_4$/P(VDF–HFP) nanocomposites, the bilayer composites exhibit greatly suppressed loss and improved breakdown strengths, as well as simultaneously enhanced energy densities and discharge efficiencies. A high breakdown strength of 472.24 kV mm^{-1}, a high energy density of 7.58 J cm^{-3} and a high discharge efficiency of 81.6% are concurrently achieved in the bilayer composite with merely 0.5 wt% $FePO_4$ nanosheets. The outstanding comprehensive energy storage performances make these nanocomposites promising candidates for advanced electrostatic capacitors. This design strategy provides an effective way to break the dilemma that high energy density is always accompanied by low discharge efficiency.

Conflicts of interest

The authors declare no conflicts of interest.

Acknowledgements

The authors acknowledge the financial support of this work from the National Natural Science Foundation of China (51773187), and the Fundamental Research Funds for the Central Universities (201961060).

References

1 Y. Cui, T. D. Zhang, Y. Feng, C. H. Zhang, Q. G. Chi, Y. Q. Zhang, Q. G. Chen, X. Wang and Q. Q. Lei, *Composites, Part B*, 2019, **177**, 107429.
2 Q. Li and S. Cheng, *IEEE Electr. Insul. Mag.*, 2020, **36**, 7–28.
3 L. Sun, Z. C. Shi, H. L. Wang, K. Zhang, D. Dastan, K. Sun and R. H. Fan, *J. Mater. Chem. A*, 2020, **8**, 5750–5757.
4 F. H. Liu, Z. Y. Li, Q. Wang and C. X. Xiong, *Polym. Adv. Technol.*, 2018, **29**, 1271–1277.
5 Y. Wang, M. G. Yao, R. Ma, Q. B. Yuan, D. S. Yang, B. Cui, C. R. Ma, M. Liu and D. W. Hu, *J. Mater. Chem. A*, 2020, **8**, 884–917.
6 H. Palneedi, M. Peddigari, G. T. Hwang, D. Y. Jeong and J. Ryu, *Adv. Funct. Mater.*, 2018, **28**, 1803665.
7 H. Luo, X. F. Zhou, C. Ellingford, Y. Zhang, S. Chen, K. C. Zhou, D. Zhang, C. R. Bowen and C. Y. Wan, *Chem. Soc. Rev.*, 2019, **48**, 4424–4465.
8 H. L. Hu, F. Zhang, S. B. Luo, W. K. Chang, J. L. Yue and C. H. Wang, *Nano Energy*, 2020, **74**, 104844.
9 Y. N. Hao, Z. P. Feng, Z. D. He, J. M. Zhang, X. M. Liu, J. Qin, L. M. Guo and K. Bi, *Mater. Des.*, 2020, **189**, 108523.
10 D. L. He, Y. Wang, X. Q. Chen and Y. Deng, *Composites, Part A*, 2017, **93**, 137–143.
11 G. Q. Zhang, D. Brannum, D. X. Dong, L. X. Tang, E. Allahyarov, S. Tang, K. Kodweis, J. K. Lee and L. Zhu, *Chem. Mater.*, 2016, **28**, 4646–4660.
12 L. L. Ren, L. J. Yang, S. Y. Zhang, H. Li, Y. Zhou, D. Ai, Z. L. Xie, X. T. Zhao, Z. R. Peng, R. J. Liao and Q. Wang, *Compos. Sci. Technol.*, 2021, **201**, 108528.
13 Z. Q. Wu, H. H. Zhou, Q. Guo, Z. G. Liu, L. Gong, Q. Y. Zhang, G. J. Zhong, Z. M. Li and Y. H. Chen, *J. Alloys Compd.*, 2020, **845**, 156171.
14 P. Yin, Z. C. Shi, L. Sun, P. T. Xie, D. Dastan, K. Sun and R. H. Fan, *Polym. Compos.*, 2021, **42**, 3000–3010.
15 M. Wang, X. R. Pan, X. D. Qi, N. Zhang, T. Huang, J. H. Yang and Y. Wang, *Compos. Commun.*, 2020, **21**, 100411.
16 S. N. Chen, S. Chen, R. Qiao, H. R. Xu, Z. J. Liu, H. Luo and D. Zhang, *Composites, Part A*, 2021, **145**, 106384.
17 H. X. Tang, Z. Zhou and H. A. Sodano, *ACS Appl. Mater. Interfaces*, 2014, **6**, 5450–5455.
18 X. R. Pan, M. Wang, X. D. Qi, N. Zhang, T. Huang, J. H. Yang and Y. Wang, *Composites, Part A*, 2020, **137**, 106032.
19 H. Chen, X. Q. Li, W. C. Yu, J. Y. Wang, Z. Q. Shi, C. X. Xiong and Q. L. Yang, *Biomacromolecules*, 2020, **21**, 2929–2937.
20 Y. J. Fu, Y. X. Wang, S. Wang, Z. D. F. Gao and C. X. Xiong, *Polym. Compos.*, 2019, **40**, 2088–2094.
21 J. Wang, Y. C. Xie, J. J. Liu, Z. C. Zhang and Y. F. Zhang, *Appl. Surf. Sci.*, 2019, **469**, 437–445.
22 Z. Wang, X. Y. Wang, Z. X. Sun, Y. B. Li, J. W. Li and Y. Shi, *Ceram. Int.*, 2019, **45**, 18356–18362.
23 J. Y. Wang, H. Chen, X. Q. Li, C. G. Zhang, W. C. Yu, L. Zhou, Q. L. Yang, Z. Q. Shi and C. X. Xiong, *Chem. Eng. J.*, 2020, **383**, 123147.
24 G. Liu, T. D. Zhang, Y. Feng, Y. Q. Zhang, C. H. Zhang, Y. Zhang, X. B. Wang, Q. G. Chi, Q. G. Chen and Q. Q. Lei, *Chem. Eng. J.*, 2020, **389**, 124443.
25 J. P. Chen, J. L. Liu, L. X. Cai, C. Y. Wang, L. L. Liu, Q. L. Yang and C. X. Xiong, *Compos. Sci. Technol.*, 2020, **200**, 108381.
26 W. J. Ji, H. Deng, C. X. Sun and Q. Fu, *Compos. Sci. Technol.*, 2019, **172**, 117–124.
27 R. M. Mishra and J. S. P. Rai, *Polym.-Plast. Technol. Mater.*, 2019, **58**, 341–347.
28 S. S. A. Shah, H. Nasir and A. Saboor, *J. Mater. Sci.: Mater. Electron.*, 2018, **29**, 402–411.
29 M. Hegde, S. Shahid, B. Norder, T. J. Dingemans and K. Nijmeijer, *Polymer*, 2015, **81**, 87–98.
30 C. H. Du, B. K. Zhu and Y. Y. Xu, *J. Mater. Sci.*, 2006, **41**, 417–421.
31 M. K. Vyas and A. Chandra, *ACS Appl. Mater. Interfaces*, 2016, **8**, 18450–18461.
32 Y. Lin, C. Sun, S. L. Zhan, Y. J. Zhang, H. B. Yang and Q. B. Yuan, *Compos. Sci. Technol.*, 2020, **199**, 108368.
33 F. Yan, H. R. Bai, Y. J. Shi, G. L. Ge, X. F. Zhou, J. F. Lin, B. Shen and J. W. Zhai, *Chem. Eng. J.*, 2021, **425**, 130669.
34 Q. Z. Sun, J. P. Wang, L. X. Zhang, P. Mao, S. J. Liu, L. Q. He, F. Kang and R. Xue, *J. Mater. Chem. C*, 2020, **8**, 7211–7220.
35 P. J. Wang, D. Zhou, J. Li, L. X. Pang, W. F. Liu, J. Z. Su, C. Singh, S. Trukhanov and A. Trukhanov, *Nano Energy*, 2020, **78**, 105247.
36 H. Li, D. Ai, L. L. Ren, B. Yao, Z. B. Han, Z. H. Shen, J. J. Wang, L. Q. Chen and Q. Wang, *Adv. Mater.*, 2019, **31**, 1900875.
37 L. L. Ren, H. Li, Z. L. Xie, D. Ai, Y. Zhou, Y. Liu, S. Y. Zhang, L. J. Yang, X. T. Zhao, Z. R. Peng, R. J. Liao and Q. Wang, *Adv. Energy Mater.*, 2021, DOI: 10.1002/aenm.202101297.
38 H. J. Ye, T. M. Lu, C. F. Xu, M. Q. Zhong and L. X. Xu, *Nanotechnology*, 2018, **29**, 095702.
39 L. Sun, Z. C. Shi, L. Liang, S. Wei, H. L. Wang, D. Dastan, K. Sun and R. H. Fan, *J. Mater. Chem. C*, 2020, **8**, 10257–10265.

40 W. D. Sun, X. J. Lu, J. Y. Jiang, X. Zhang, P. H. Hu, M. Li, Y. H. Lin, C. W. Nan and Y. Shen, *J. Appl. Phys.*, 2017, **121**, 244101.
41 D. Zhang, W. W. Liu, R. Guo, K. C. Zhou and H. Luo, *Adv. Sci.*, 2018, **5**, 1700512.
42 W. Y. Li, Z. Q. Song, J. M. Zhong, J. Qian, Z. Y. Tan, X. Y. Wu, H. Y. Chu, W. Nie and X. H. Ran, *J. Mater. Chem. C*, 2019, **7**, 10371–10378.
43 P. Mao, J. P. Wang, L. X. Zhang, Q. Z. Sun, X. X. Liu, L. Q. He, S. J. Liu, S. W. Zhang and H. Gong, *Phys. Chem. Chem. Phys.*, 2020, **22**, 13143–13153.
44 F. H. Liu, Q. Li, Z. Y. Li, Y. Liu, L. J. Dong, C. X. Xiong and Q. Wang, *Compos. Sci. Technol.*, 2017, **142**, 139–144.
45 H. J. Ye, X. H. Zhang, C. F. Xu, B. Han and L. X. Xu, *J. Mater. Chem. C*, 2018, **6**, 11144–11155.
46 S. N. Chen, X. M. Yan, W. T. Liu, R. Qiao, S. Chen, H. Luo and D. Zhang, *Chem. Eng. J.*, 2020, **401**, 126095.
47 M. A. Marwat, B. Xie, Y. W. Zhu, P. Y. Fan, K. Liu, M. Shen, M. Ashtar, S. Kongparakul, C. Samart and H. B. Zhang, *Colloids Surf., A*, 2019, **581**, 123802.

